energy&fuels

Article

pubs.acs.org/EF

Raman Spectroscopy of Soot Sampled in High-Pressure Diffusion Flames

Mario Commodo,*[,†] Peter H. Joo,*[,‡] Gianluigi De Falco,[†] Patrizia Minutolo,[†] Andrea D'Anna,[§] and Ömer L. Gülder[‡]

[†]Istituto di Ricerche sulla Combustione, CNR, Piazzale Tecchio 80, 80125 Napoli, Italy

[‡]Institute for Aerospace Studies, University of Toronto, 4925 Dufferin Street, Toronto, Ontario, Canada M3H 5T6

[§]Dipartimento di Ingegneria Chimica, dei Materiali e della Produzione Industriale, Università degli Studi di Napoli Federico II, Piazzale Tecchio 80, 80125 Napoli, Italy

ABSTRACT: The effect of pressure on soot particle nanostructure has been investigated by Raman spectroscopy. For the first time soot samples produced in a set of coflow methane−air laminar diffusion flames stabilized in a high-pressure combustion chamber, and collected by thermophoresis, have been analyzed to obtain chemical/structural information. The first-order Raman spectra of soot particles collected at several elevated pressures have been analyzed and compared. As a result, within the investigated range of pressures, i.e., from 10 to 20 bar, our measurements show that soot nanostructure does not depend on the pressure conditions. Changes in soot nanostructure were only observed as a function of flame residence time. The results herein presented are particularly relevant by considering the importance of nanostructure on the soot reactivity toward oxidation and on the fact that soot from practical combustion devices is mostly produced at high pressure.

INTRODUCTION

Soot formation in flames has long been a subject of experimental, numerical, and theoretical investigations.[1,2] Carbonaceous soot nanoparticles produced by combustion systems are of significant concern because of their negative effects on human health[3,4] and air quality, especially in urban areas. Furthermore, the emission of soot particles in the atmosphere has also complex environmental and climate implications.[5,6] In previous studies, efforts to develop more efficient and less polluting combustion technologies were focused on the improvements of our understanding of soot formation mechanisms in fuel-rich combustion conditions. Nonetheless, a clear description of the chemical and physical pathways of the soot formation processes in flames has not been accomplished. The task of providing a clear description of soot formation requires a comprehensive understanding of gas-phase free radical reactions, benzene and other larger polyaromatic hydrocarbons formation, particle nucleation, particle growth through surface gas-to-solid reactions, and the physical particle coagulation/coalescence processes.[7−10] Furthermore, carbonization and oxidation reactions provide additional complications to the overall soot formation mechanism. The elusive nature of the physicochemical evolution of the soot in flames is further complicated by the fact that all the chemical and physical phenomena involved during the soot formation process are strongly dependent on a large variety of parameters, including fuel chemical composition, burning configuration, residence time, flame temperature, and the pressure at which combustion takes place. Although soot production in practical combustion systems mainly occurs at high pressure, most of the previous studies on soot formation have been primarily focused on flames at atmospheric pressure.[11]

Soot belongs to a class of carbon particles whose main characteristics, i.e., volume fraction, physical size, nanostructure, and chemical composition, change significantly as a function of the combustion parameters mentioned above. This leads to a wide range of characteristics of the soot particles, such as their reactivity toward oxidation[12,13] and their optical properties[10] that have important practical implications. For instance, soot oxidative reactivity is a critical factor for the operation/regeneration of the particulate traps that are currently used in diesel engines as exhaust after-treatment systems. However, information on the effect of pressure on the soot morphology, chemical composition, and the nanostructure is quite scarce and suffers from a lack of discrimination of competing parameters that might influence the soot production. Interpretation of the primary soot size and aggregate morphological data evaluated from in-cylinder diesel engine sampling experiments pose serious challenges due to the inherent unsteady nature of the combustion events in reciprocating engines.[14−16] It may not be possible to assess the influence of engine operating variables on soot processes independently. For example, changing the fuel injection pressure affects the spray characteristics, ignition delay, variations in local equivalence ratios, and residence time of soot formation, in addition to the potential impact on local turbulence structure in varying pressure (and temperature) conditions. Similar concerns are valid to assess the influence of combustion pressure, which cannot be kept constant, on soot characteristics in diesel engine combustion.

Pressure has a considerable effect on soot formation. The rate of soot formation is increased significantly with increasing

Received: June 12, 2017
Revised: July 26, 2017
Published: August 2, 2017

DOI: 10.1021/acs.energyfuels.7b01674
Energy Fuels 2017, 31, 10158−10164

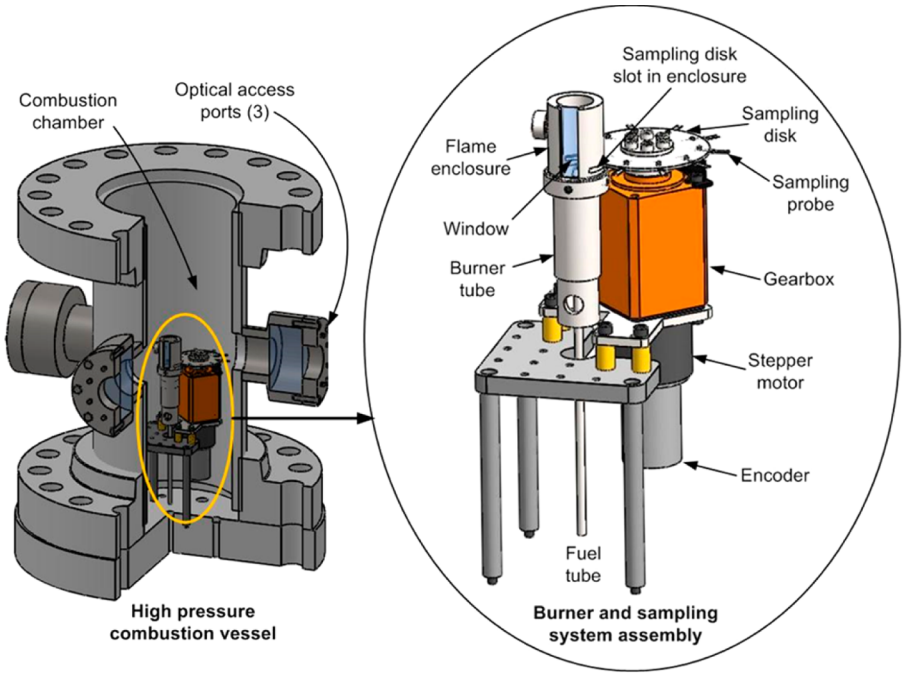

Figure 1. Three-dimensional illustrative rendering of the high-pressure combustion chamber, thermophoretic sampling system, and the burner assembly. The details of the sampling system and the burner assembly are shown in the blow-out view on the right. Illustration adapted with permission from ref 38.

pressure due to increased rate of collisions between the large PAH molecules that lead to soot particle nuclei. It should be noted that high-performance aviation propulsion systems and terrestrial combustion engines operate at superatmospheric pressures, up to 40−50 bar in gas turbine engines and exceeding 100 bar in diesel engines. Thus, a comprehensive understanding of the influence of pressure on soot formation and on the morphological structure of soot is needed to provide innovative tools that could be used for soot reduction and abatement solutions in these combustion devices. Yet, most of the soot measurements under elevated pressure conditions that are available in the literature are not tractable measurements in that one or two important parameters were not kept constant. For instance, in the work by Flower and Bowman[17] with ethylene diffusion flames at pressures up to 2.5 bar, the primary soot particle diameters and the soot number density (particles per soot aggregate) increased with increasing pressure. They attribute these observations to being a result of increased surface growth rates and particle generation rates at elevated pressures. In their work, however, the fuel mass flow rate increased linearly with increasing pressure by having the fuel exit velocity fixed for all pressures. Then the growth of the soot particles and the increased soot number density were not only affected by pressure but also from the increased supply of carbon that contributed to the soot particle growth and soot number density. Therefore, it is not possible to ascertain the effect of pressure without removing the effect of increased flow of carbon from the fuel stream. Similarly, investigations on the effect of pressure on the primary soot particle diameter by Heidermann et al.[18] and Kim et al.[19] also suffer from increased fuel mass flow rate with increasing pressure which makes it difficult, if possible at all, to isolate and ascertain the effect of pressure only.

Experimentally, the main characteristics of the soot particles produced in fuel-rich combustion have been investigated by both in situ[9,10] and ex situ characterization techniques.[11] In situ measurements, such as laser-based optical diagnostics, light extinction, and emission spectroscopy, have been frequently used in combustion to determine the particle concentrations and primary soot particle size, thus providing functional sets of data to support computational modeling of soot formation in flames. However, the applicability of the optical techniques at high pressures is uncertain. Thomson et al.[20] measured the primary soot particle size using laser-induced incandescence (LII) in a sooting methane−air laminar diffusion flame at pressures up to 40 bar and reported that the primary soot particles increased in diameter with increasing pressure. As noted by the authors, however, what is measured using the LII technique is an effective primary soot particle size and not the actual primary soot particle size because the shielding effect on heat conduction between the agglomerates and the surrounding gas is neglected. In a more recent work, Steinmetz et al.[21] used light-extinction and -scattering technique on nitrogen-diluted ethylene−air diffusion flames at pressures up to 16 bar and measured the primary soot particle size. However, they also indicate a great deal of experimental difficulty due to high-pressure beam steering with the light-extinction technique and that what is measured is an intermediate size between that of the primary soot particles and the soot aggregates.

Another approach to soot investigations is to physically collect the soot particles in the flame and expose them to a large variety of analytical techniques. In this case, most often a cold substrate is inserted for a very short residence time, i.e., usually a few or tens of milliseconds, into the flame and, as a result of the different temperatures between the combustion gases and the substrate, particles are forced by thermophoresis to impact on the substrate.[22] Thermophoretic sampling has proven to be a valuable method capable of producing useful soot samples for many analytical techniques, including Raman spectroscopy.[23,24] Very recently, thermophoretic sampling of

DOI: 10.1021/acs.energyfuels.7b01674
Energy Fuels 2017, 31, 10158−10164

soot has been successfully implemented also at elevated pressures.[25]

In recent years, the extensive use of Raman spectroscopy in carbon-based material studies has led to a significant progress in the understanding of the Raman processes involved. As a result, Raman scattering has emerged as a remarkable and powerful tool for gaining chemical, structural, and electronic information on many carbon-based materials.[26] In this context, Raman spectroscopy has also become a common analytical method used to gain information on soot micro-/nanostructure. Particularly, starting from the work of Sadezky et al.,[27] Raman spectroscopy has already been adopted to study engine and surrogate soot samples,[28,29] soot oxidation reactivity,[30,31] and flame-formed soot particles, along with their physicochemical transformation during the formation and evolution in the flame.[32−36]

In this work, the nanostructure of soot particles produced in diffusion flames at elevated pressures has been investigated by Raman spectroscopy. The aim of this work was to achieve a better understanding on the effect of pressure on the nanostructure of the soot particles. To the best of our knowledge, for the first time soot particles have been collected by thermophoresis from a set of laminar diffusion flames stabilized at different high pressures, i.e., between 10 and 20 bar, and analyzed in terms of their nanostructure.

EXPERIMENTAL SECTION

For collecting soot samples thermophoretically, we used a high-pressure combustion chamber capable of stabilizing laminar diffusion flames on a coflow burner. The high-pressure combustion chamber, housing the burner and the integrated thermophoretic soot sampling system, used for this work, has been described previously in detail[37,38] and only a brief description is provided here. The high-pressure combustion chamber was designed to operate at pressures up to 110 bar, with an internal diameter and height of 24 and 60 cm, respectively. The coflow laminar diffusion flame installed in the high-pressure chamber has an exit diameter of 3 mm. In the flow passage of the burner exit a porous metal insert provides a top-hat velocity profile. The inner diameter of the coflow air nozzle is 25 mm, and the air nozzle is also fitted with a porous metal insert to minimize the flow nonuniformities as the air flow exits the burner. A cutaway view of the high-pressure combustion chamber and the main components of the thermophoretic sampling system are shown in Figure 1. The thermophoretic sampling system consists of a circular sampling disk, a motor drive, and a programmable control system. The circular sampling disk is fitted with 10 probe arms that each extends radially outward, Figure 1. The programmable control system regulates the rotation of the sampling disk as the probe arm travels through the flame cross-section at a given height above the burner rim. After the probe arm completes sampling through the flame, the sampling disk comes to a complete stop to allow the flame to recover from the disturbances caused by the probe arm. This process is repeated for the next sampling probe once the flame becomes stable again.

To keep measurements at different pressures tractable, fuel and air mass flow rates were kept constant at all pressures considered. The methane flow rate at all pressure levels was kept as 0.55 mg/s which corresponds to a carbon mass flow rate of 0.41 mg/s. At all pressures, a constant coflow air mass flow of 0.34 g/s is provided. Pressures investigated were P = 10, 15, and 20 bar. The flame height is about 9 mm; see the pictures depicted in Figure 2. Soot particles were sampled at three flame positions, h = 3, 5, and 8 mm above the burner rim. Note that in laminar coflow diffusion flames at elevated pressures, the flame height, hence the residence time, is independent of the pressure, and thus measurements can be compared at the same heights above the burner exit.[11]

Samples for Raman spectroscopy measurements were collected by multiple insertions of the substrate into the flame to accumulate enough material for the analysis. (Note: TEM grids with an outer diameter of 3 mm were used in our case; however, any substrate sufficiently covered by soot could be used instead). The sample collection time of the single sweep of the thermophoretic probe was 28.3 ms. However, to collect sufficient amount of soot on the TEM grid, multiple sweeps of the probe were conducted providing enough time between the sweeps to let the flame recover from the probe disturbance and to prevent the grid temperature from increasing. As a result, the total soot collection time ranged between 340 ms and about 3400 ms, depending on the soot concentration in the flame which is being interrogated.

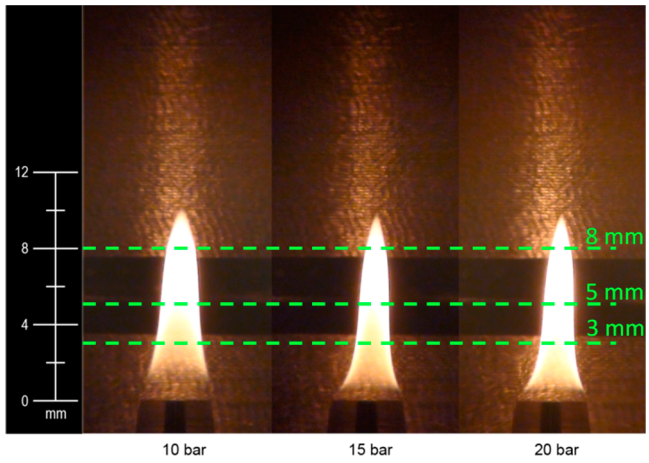

Figure 2. Images of the investigated laminar coflow methane−air flames at different pressures.

Sampled particles were analyzed by Raman spectroscopy positioning the grids directly under the Raman microscope (Horiba XploRA) equipped with a 100× objective (NA0.9, Olympus). The laser source was a frequency doubled Nd:YAG laser (λ = 532 nm, 12 mW maximum laser power at the sample). The calibration of the system was performed against the Stokes Raman signal of pure silicon at 520 cm^{-1}. A 200 μm pinhole was used for confocal photon collection. The power of the excitation laser beam and the exposure time were adjusted to avoid structural changes of the sample due to thermal decomposition. Spectra were obtained with a laser beam power of 1%, and an accumulation-exposure time of five cycles of 20 s each. For each soot sample deposited on a TEM grid several spots were randomly selected and averaged to obtain a statistically relevant Raman spectrum.

RESULTS AND DISCUSSION

A picture of the flames at different pressure is reported in Figure 2. The green lines highlight the three distances above the burner nozzle at which soot particles have been collected.

Raman spectroscopy allows obtaining chemical/structural information on carbon materials, including soot particles. A thorough description of the Raman spectroscopy analysis of soot particles can be found elsewhere[23,24,27−36] and is here briefly reported. The first-order Raman spectrum, 1000−1800 cm^{-1}, of the soot samples collected in flame at h = 8 mm and P = 15 bar is reported in Figure 3. It presents the typical characteristics of any disordered carbonaceous materials: within this spectral region, two main bands are commonly present, one centered at about 1600 cm^{-1} designed as the G band and the other centered at about 1350 cm^{-1} and named as D band.

The high sensitivity of the technique, in probing chemical/structural information on carbon materials, lies in the fact that the presence of defects in the sp^2 aromatic network allows the activation of the Raman D mode at ∼1350 cm^{-1}, prohibited in the perfect hexagonal lattice.[26] Conversely, the G band, at

DOI: 10.1021/acs.energyfuels.7b01674
Energy Fuels 2017, 31, 10158−10164

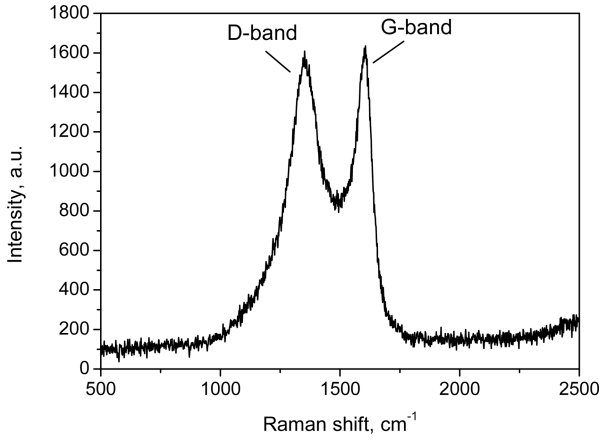

Figure 3. First-order Raman spectrum of a flame-soot sample.

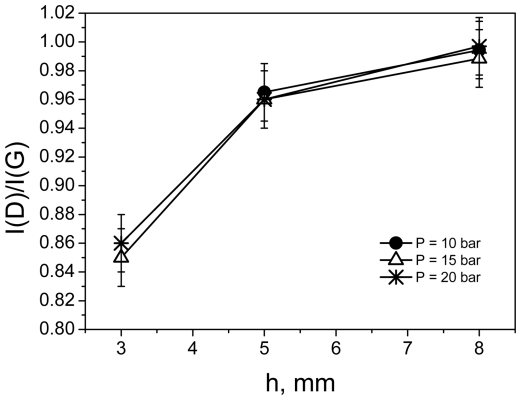

Figure 4. $I(D)/I(G)$ ratio obtained from the Raman spectra of the soot particles collected on the TEM grids at different flame heights and pressures.

~1600 cm^{-1}, which is due to every sp^2 bond, is mostly insensitive to defects only presenting small changes in width and position of the maximum as a function of the different carbon structures.

The ratio of the D and G peak intensities has been widely used to estimate the in-plane correlation length of the aromatic islands, L_a, i.e., the size of graphitic domains.[26] Tuinstra and Koening[39] studied the Raman spectrum of graphite and microcrystalline graphite and showed that for these materials the intensity ratio $I(D)/I(G)$ was inversely proportional to L_a.[39] This inverse relationship has been successively verified down to a minimum of L_a corresponding to about 2−3 nm, where $I(D)/I(G)$ reaches a maximum value.[26,40] When L_a further decreases, i.e., for highly disordered materials, $I(D)/I(G)$ decreases to zero. Indeed, for highly amorphous carbon materials, $I(D)/I(G)$ represents the probability of finding aromatic sp^2 hybridized carbon with respect to the total sp^2 hybridized carbon.[40] Such a nonmonotonic trend of $I(D)/I(G)$ versus L_a has been described in detail by Ferrari and Basko[26] and by Martins Ferreira et al.[40] These two regions in the $I(D)/I(G)$ as a function of L_a can be discriminated considering the full width at half-maximum, FWHM, of the two Raman lines, which have been demonstrated to become wider with increasing disorder.[40] For flame-generated soot particles the low-L_a regime, i.e., $L_a <$ 2−3 nm, usually applies.[23,24,33,34] This is further corroborated by the fact that the width of the Raman lines in the spectrum shown in Figure 3, as well as in any of the other soot Raman spectra measured in this work, is of the order of 100 cm^{-1}. This is typical of the highly disordered/amorphous regime, i.e., very small size of the graphite crystallites, for which the following empirical expression has been found to correlate L_a with the relative intensity of the two Raman bands:[26]

$$L_a{}^2/\mathrm{nm}^2 = 5.4 \times 10^{-2}(E_L{}^4/\mathrm{eV}^4)\frac{I(D)}{I(G)} \quad (1)$$

where E_L is the energy of the incident photon.

In Figure 4 the ratio $I(D)/I(G)$, obtained from the measured Raman spectra, is plotted as a function of the flame height for the three investigated pressures, i.e., 10, 15, and 20 bar. For flames stabilized at pressures lower than 10 bar, soot volume fraction was too small for sampling enough material on the substrates by thermophoresis to perform Raman spectroscopy measurements. This was also the case for 10 bar and h = 3 mm. All the other TEM grids were sufficiently covered by soot particles for performing Raman measurements. The obtained $I(D)/I(G)$ data are reported in Figure 4, clearly showing that the major effect on particle nanostructure is given by the residence times in the flame. Indeed, regardless of the pressure, moving from 3 to 8 mm the $I(D)/I(G)$ ratio noticeably increases, thus denoting an increase in the graphitic order of the soot particles. Particularly, by using eq 1 the average size of the aromatic domains changes by about 10%, increasing from 1.15 nm at h = 3 mm ($I(D)/I(G) \approx 0.85$) to about 1.3 nm for the soot collected at 8 mm ($I(D)/I(G) \approx 1.00$).

An average error of ±0.02 has been evaluated for the $I(D)/I(G)$ ratio. Within this error, the $I(D)/I(G)$ plots follow the same trend as a function of the three investigated pressures. As a result, soot particles change their carbon nanostructure mainly for the different residence times. This is particularly relevant in the central zone of the flame, from 3 to 5 mm, but the aromatic domains continue growing, also approaching the oxidation zone, h = 8 mm. A similar trend was also observed for soot particles collected from an atmospheric pressure non-smoking ethylene diffusion flame by means of laser microprobe mass spectrometry, LMMS, by Dobbins et al.[41] The authors suggested that the carbonization process observed in their flame was due to the dehydrogenation of the PAH species formed in the lower flame. Nevertheless, the influence of other processes during the soot evolution in the flame,[8] such as the surface growth, particle coagulation, and oxidation, cannot be excluded. Recently, Toth et al.,[42] in a study aimed at investigating the effect of oxidation pressure on soot nanostructure, observed a slight increase of the size of graphene layers of several flame-soot particles exposed to increased oxidation pressures. Within the set of high-pressure laminar diffusion flames investigated in our study the 8 mm height corresponds to the onset of the flame oxidation region; thus, changes in soot structure were at least expected in this flame region. Future work is certainly needed to better address this point.

Although D and G bands represent the most prominent features in the first-order spectrum of soot and other amorphous carbon materials, the presence of other Raman lines can be taken into account.[19−27,31−33] However, because of the superposition of these lines, the Raman spectrum needs to be fitted with a multiple-line function to evidence each contribution. In this work the Raman spectra of soot were fitted with four Lorentzian functions, labeled as D″, D, G, and D′ at about 1200, 1350, 1590, and 1620 cm^{-1}, respectively, and one Gaussian shaped curve, D3, at about 1530 cm^{-1}, following the procedure reported elsewhere.[27−35,43−45] For clarity, Table

DOI: 10.1021/acs.energyfuels.7b01674
Energy Fuels 2017, 31, 10158−10164

Table 1. Raman Modes Attributions

band	curve fit	attribution
G	Lorentzian	due to every sp^2 bond; characteristic of crystalline graphite/graphene
D	Lorentzian	due to aromatic sp^2 bond; presence of defects allows the observation of this mode
D′	Lorentzian	mode activated by defects; related to edge carbons
D″	Lorentzian	may indicate the presence of polyenic chains attached to the edge of graphite crystallites or ionic impurities (attribution is poorly understood)
D3	Gaussian	commonly associated with amorphous carbon involving organic molecules, fragments, functional groups, and/or the inclusion of odd-membered ring structures, curvature (attribution is poorly understood)

1 reports a short description of the attributions of the different Raman bands based on current literature.[27−35,43−45]

A typical set of fits to the Raman spectrum of soot collected at h = 5 mm, and pressure of 15 bar, is depicted in Figure 5.

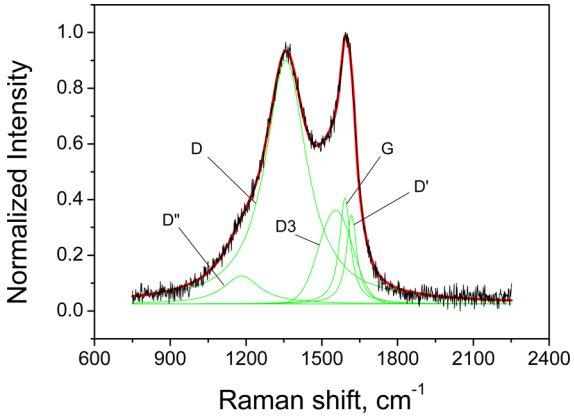

Figure 5. Measured Raman spectra of soot particles collected at 5 mm above the burner in the diffusion flame stabilized at 15 bar (black line). Green lines represent the different Raman lines obtained from the fitting procedures. Red line is the cumulative fit line.

The most relevant trends of the fit parameters are shown in Figure 6 for soot collected in flames at 15 and 20 bar for the three investigated heights above the burner. The main observations are as follows:

(a) There is a decrease in FWHM of D and G lines with the residence time in the flame, which indicates that soot at increasing position along the flame is becoming more graphitic.

(b) The decrease in the position of the G band, labeled as Pos G, is consistent with an increase of L_a, thus consistent with the $I(D)/I(G)$ trends discussed above. Indeed, it is known that this value is not unique since it is very sensitive to the carbon network. Specifically, in perfect graphite the maximum of the G band is positioned at ∼1580 cm^{-1} while this value increases with disorder saturating at about 1600 cm^{-1} in carbon materials made of only aromatic rings such as in nanocrystalline graphite.[46] Thus, the observed trend in the position of the G band, decreasing as a function of h, indicates a graphitization trend of the soot particles comparable to the transformation of nanocrystalline graphite to graphite.

(c) The ratios of the band areas, $A(D3)/A(G)$ and $A(D'')/A(G)$, both show a maximum for soot particles at 5 mm. It is worth noting that Raman spectroscopy is very sensitive to graphitization and amorphization processes occurring in a disordered carbonaceous material since the Raman bands change both in intensity and line width. To take into account the whole scattering process, the area under the peak can be considered as reported by Martins Ferreira et al.[40] However, all parameters add complementary information. Indeed, although the bandwidth gives information on the structural disorder, the intensity is more representative of the resonant process. The disorder associated with bands D3 and D″ is quite low at 3 mm, i.e., at the early stages of soot formation. The increase of these two bands observed while soot particles evolve in the flame, i.e., from 3 to 5 mm, seems to be indicative of an increase of a structural disorder typical of a distorted graphitic lattice or formation of side or cross-linking chains between aromatic planes. It may be, for instance, related to an enhanced deformation of the aromatic planes in the aged soot as probably due to the formation of five-memberd rings. The further evolution of the soot particles, i.e., from 5 to 8 mm, occurs approaching the flame oxidation zone and results in a relevant reduction of such amorphous phase and a further slight increase of size of the aromatic domains. This latter aspect is consistent with several previous investigations of the effect of oxidation on soot nanostructure.[42]

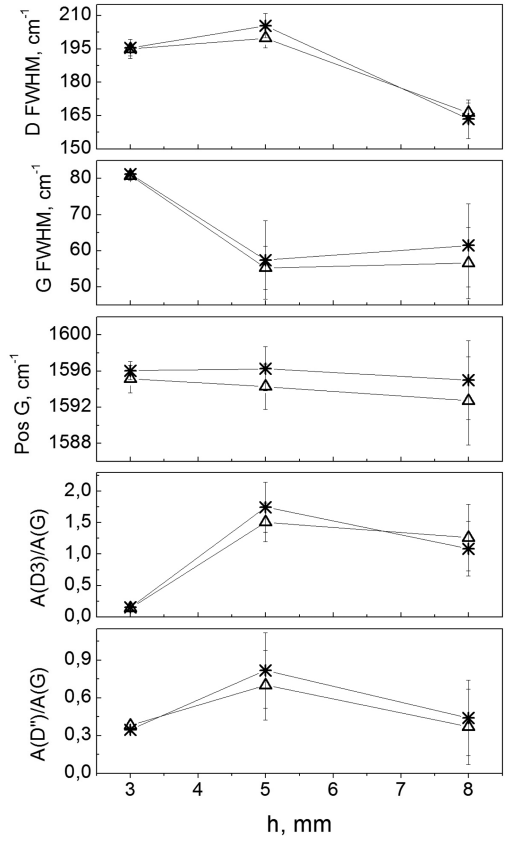

Figure 6. Variations of certain fit parameters as a function of sampling height in the flame at P = 15 (blank triangles) and 20 bar (stars).

In addition to the Raman D and G bands, typical of amorphous or disordered carbon materials and nanographite, the Raman spectra of soot particles often present a photoluminescence background (PL), as shown in Figure 7. PL background in Raman spectrum has been reported for

DOI: 10.1021/acs.energyfuels.7b01674
Energy Fuels 2017, 31, 10158−10164

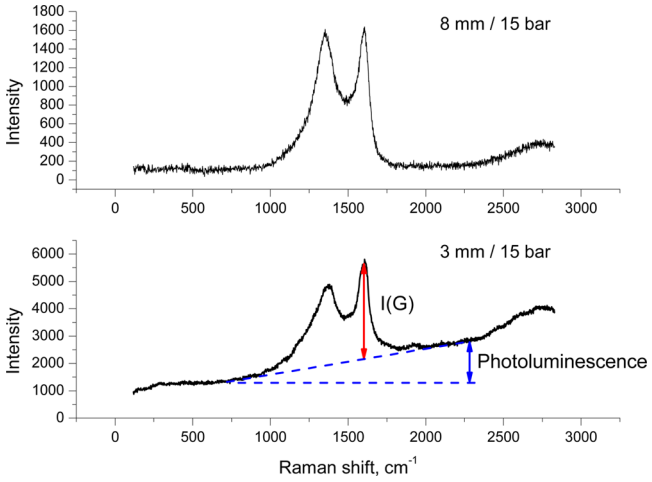

Figure 7. Raw Raman spectra of soot particles collected at 3 and 8 mm at P = 15 bar.

hydrogenated carbon due to the radiative recombination of electrons and holes in the localized states created by sp^2 clusters.[47] Following the procedure reported by Casiraghi et al.[47] the PL intensity was measured by evaluating the slope of the PL linear background, m, divided by the intensity of the Raman line at about 1600 cm^{-1} (the G mode), which is due to the total sp^2 in the sample. Therefore, such a method furnishes the amount of fluorescing component with respect to the total sp^2 carbon present in the analyzed sample. To some extent, the ratio $m/I(G)$ can be considered as an indication of the relative content of the organic carbon, OC, with respect to the total sp^2 carbon in the collected soot particles. Also note that a contribution to the PL background from adsorbed gas-phase PAH molecules on soot particles cannot be excluded, although these molecules should have a molecular mass larger than 1000 Da to be collected by thermophoresis.[48]

Casiraghi et al.,[47] also found an empirical equation that can be used for determining the hydrogen to carbon atomic ratio based on the measured $m/I(G)$:

$$H/(at.\ \%) = 21.7 + 16.6 \log\left\{\frac{m}{I(G)}/\mu m\right\} \quad (2)$$

It should be noted that eq 2 was obtained using Raman spectra acquired using λ = 514.5 nm as excitation laser source, fairly close the one used in our study; i.e., λ = 532 nm. This shift in the excitation wavelength, which mostly affects the term of photoluminescence, may introduce some error when attempting to evaluate the hydrogen content in soot particles. Nevertheless, in our case, the application of eq 2 allows one to get qualitative information on the evolution of the chemical composition of the collected soot particles along the flames.

Figure 8a reports the ratio between the slope of the photoluminescence background and the intensity of the G band versus the height above the burner. This ratio, which is related to the amount of organic carbon in soot particles and/or to the percentage of hydrogen in the carbon material, differs significantly for soot collected at different residence times. Particularly, the organic content is higher at a lower point in the flame and it decreases with increasing height above the burner. As a result, the H/C ratio decreases with increasing sampling height, as estimated by eq 2 and shown in Figure 8b. No effect

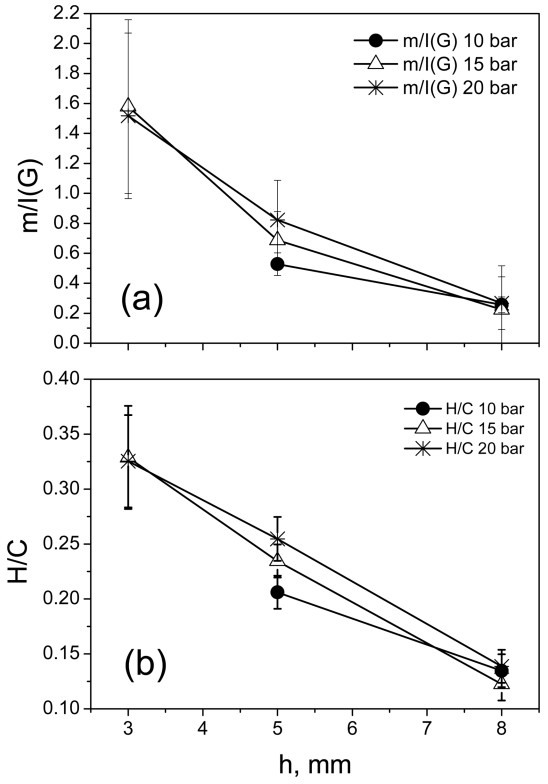

Figure 8. $m/I(G)$ versus sampling height within the flame at different pressures (a); H/C ratio derived from the measured $m/I(G)$ values using eq 2 (b).

is evidenced by changing the pressure in the range between 10 and 20 bar.

CONCLUSIONS

Soot collected by thermophoresis from several methane diffusion flames stabilized at elevated pressures, i.e., between 10 and 20 bar, have been analyzed by Raman spectroscopy. The first-order Raman spectra of several soot samples collected at three heights above the burner and at different elevated pressures have been collected and analyzed in order to probe information on their nanostructure. The analysis consisted of the evaluation of the ratio of the two main features of the Raman spectra, $I(D)/I(G)$, that is well-known to be related to the in-plane correlation length, L_a, of the aromatic planes constituting the nanographite domains forming the soot particles. In addition, Raman spectra were also analyzed by multiple-line fitting procedure that allows a more accurate evaluation of the soot nanostructure. Finally, photoluminescence background was considered in relation to the intensity of the G band as an indication of the relative contribution of the organic carbon fraction over the total sp^2 carbon constituting the collected material. Overall, soot particles examined in this study showed a progressive graphitization along the flame from the particle formation up to the oxidation region. In the examined range of pressure, 10−20 bar, no dependence on pressure was evidenced. Further works are planned to investigate the pressure effect down to the atmospheric pressure, and deeply in the oxidation zone up to the flame tip, where probably larger changes in the soot nanostructure may be expected.

DOI: 10.1021/acs.energyfuels.7b01674
Energy Fuels 2017, 31, 10158−10164

AUTHOR INFORMATION

Corresponding Authors

*E-mail: commodo@irc.cnr.it (M.C.).
*E-mail: peter@utias.utoronto.ca (P.H.J.).

ORCID

Mario Commodo: 0000-0002-3908-2096
Patrizia Minutolo: 0000-0001-7837-7199
Andrea D'Anna: 0000-0001-9018-3637
Ömer L. Gülder: 0000-0001-5342-9837

Notes

The authors declare no competing financial interest.

ACKNOWLEDGMENTS

This work was financially supported by the Natural Sciences and Engineering Research Council of Canada through a discovery grant (251116-2012) and by the Accordo CNR-MSE Ricerca di sistema elettrico nazionale - Project "Efficienza energetica e risparmio di energia negli usi finali elettrici e interazione con altri vettori energetici" PAR 2015−2017.

REFERENCES

(1) Haynes, B. S.; Wagner, H. Gg. *Prog. Energy Combust. Sci.* **1981**, *7*, 229−273.
(2) Richter, H.; Howard, J. B. *Prog. Energy Combust. Sci.* **2000**, *26*, 565−608.
(3) Kennedy, I. M. *Proc. Combust. Inst.* **2007**, *31*, 2757−2770.
(4) Pedata, P.; Stoeger, T.; Zimmermann, R.; Peters, A.; Oberdörster, G.; D'Anna, A. *Part. Fibre Toxicol.* **2015**, *12*, 34.
(5) Lu, Z.; Streets, D. G.; Winijkul, E.; Yan, F.; Chen, Y.; Bond, T. C.; Feng, Y.; Dubey, M. K.; Liu, S.; Pinto, J. P.; Carmichael, G. R. *Environ. Sci. Technol.* **2015**, *49*, 4868−4877.
(6) Charlson, R. J.; Schwartz, S. E.; Hales, J. M.; Cess, R. D.; Coakley, J. A.; Hansen, J. E.; Hofmann, D. J. *Science* **1992**, *255*, 423−430.
(7) D'Anna, A. *Proc. Combust. Inst.* **2009**, *32*, 593−613.
(8) Wang, H. *Proc. Combust. Inst.* **2011**, *33*, 41−67.
(9) Desgroux, P.; Mercier, X.; Thomson, K. A. *Proc. Combust. Inst.* **2013**, *34*, 1713−1738.
(10) Michelsen, H. A. *Proc. Combust. Inst.* **2017**, *36*, 717−735.
(11) Karatas, A. E.; Gülder, Ö. L. *Prog. Energy Combust. Sci.* **2012**, *38*, 818−845.
(12) Vander Wal, R. L.; Tomasek, A. J. *Combust. Flame* **2003**, *134*, 1−9.
(13) Jaramillo, I. C.; Gaddam, C. K.; Vander Wal, R. L.; Lighty, J. S. *Combust. Flame* **2015**, *162*, 1848−1856.
(14) Lee, K. O.; Cole, R.; Sekar, R.; Choi, M. Y.; Kang, J. S.; Bae, C. S.; Shin, H. D. *Proc. Combust. Inst.* **2002**, *29*, 647−653.
(15) Leidenberger, U.; Mühlbauer, W.; Lorenz, S.; Lehmann, S.; Brüggemann, D. *Combust. Sci. Technol.* **2012**, *184*, 1−15.
(16) Mathis, U.; Mohr, M.; Kaegi, R.; Bertola, A.; Boulouchos, K. *Environ. Sci. Technol.* **2005**, *39*, 1887−1892.
(17) Flower, W. L.; Bowman, C. T. *Symp. Combust., [Proc.]* **1985**, *20*, 1035−1044.
(18) Heidermann, Th.; Jander, H.; Wagner, H. Gg. *Phys. Chem. Chem. Phys.* **1999**, *1*, 3497−3502.
(19) Kim, C. H.; Xu, F.; Faeth, G. M. *Combust. Flame* **2008**, *152*, 301−316.
(20) Thomson, K.; Snelling, D.; Smallwood, G.; Liu, F. *Appl. Phys. B: Lasers Opt.* **2006**, *83*, 469−475.
(21) Steinmetz, S. A.; Fang, T.; Roberts, W. L. *Combust. Flame* **2016**, *169*, 85−93.
(22) Köylü, Ü.Ö.; McEnally, C. S.; Rosner, D. E.; Pfefferle, L. D. *Combust. Flame* **1997**, *110*, 494−507.
(23) Herdman, J. D.; Connelly, B. C.; Smooke, M. D.; Long, M. B.; Miller, J. H. *Carbon* **2011**, *49*, 5298−5311.
(24) De Falco, G.; Commodo, M.; D'Anna, A.; Minutolo, P. *Proc. Combust. Inst.* **2017**, *36*, 763−770.
(25) Vargas, A. M.; Gülder, Ö.L. *Proc. Combust. Inst.* **2017**, *36*, 975−984.
(26) Ferrari, A. C.; Basko, D. M. *Nat. Nanotechnol.* **2013**, *8*, 235−246.
(27) Sadezky, A.; Muckenhuber, H.; Grothe, H.; Niessner, R.; Pöschl, U. *Carbon* **2005**, *43*, 1731−1742.
(28) Ivleva, N. P.; Messerer, A.; Yang, X.; Niessner, R.; Pöschl, U. *Environ. Sci. Technol.* **2007**, *41*, 3702−3707.
(29) Lapuerta, M.; Oliva, F.; Agudelo, J. R.; Stitt, J. P. *Combust. Sci. Technol.* **2011**, *183*, 1203−1220.
(30) Schmid, J.; Grob, B.; Niessner, R.; Ivleva, N. P. *Anal. Chem.* **2011**, *83*, 1173−1179.
(31) Seong, H. J.; Boehman, A. L. *Energy Fuels* **2013**, *27*, 1613−1624.
(32) Dippel, B.; Jander, H.; Heintzenberg, J. *Phys. Chem. Chem. Phys.* **1999**, *1*, 4707−4712.
(33) Commodo, M.; Tessitore, G.; De Falco, G.; Bruno, A.; Minutolo, P.; D'Anna, A. *Proc. Combust. Inst.* **2015**, *35*, 1795−1802.
(34) Commodo, M.; De Falco, G.; Bruno, A.; Borriello, C.; Minutolo, P.; D'Anna, A. *Combust. Flame* **2015**, *162*, 3854−3863.
(35) Russo, C.; Ciajolo, A. *Combust. Flame* **2015**, *162*, 2431−2441.
(36) Commodo, M.; D'Anna, A.; De Falco, G.; Larciprete, R.; Minutolo, P. *Combust. Flame* **2017**, *181*, 188−197.
(37) Joo, P. H.; Charest, M. R.; Groth, C. P.; Gülder, Ö. L. *Combust. Flame* **2013**, *160*, 1990−1998.
(38) Vargas, A. M.; Gülder, Ö. L. *Rev. Sci. Instrum.* **2016**, *87*, 055101.
(39) Tuinstra, F.; Koenig, J. L. *J. Chem. Phys.* **1970**, *53*, 1126−1130.
(40) Martins Ferreira, E. H.; Moutinho, M. V. O.; Stavale, F.; Lucchese, M. M.; Capaz, R. B.; Achete, C. A.; Jorio, A. *Phys. Rev. B: Condens. Matter Mater. Phys.* **2010**, *82*, 125429.
(41) Dobbins, R. A.; Fletcher, R. A.; Lu, W. Laser Microprobe Analysis of Soot Precursor Particles and Carbonaceous Soot. *Combust. Flame* **1995**, *100*, 301−309.
(42) Toth, P.; Palotas, A. B.; Ring, T. A.; Eddings, E. G.; Vander Wal, R.; Lighty, J. S. *Combust. Flame* **2015**, *162*, 2422−2430.
(43) Sheng, C. *Fuel* **2007**, *86*, 2316−2324.
(44) De Falco, G.; Commodo, M.; Bonavolontà, C.; Pepe, G.; Minutolo, P.; D'Anna, A. *Combust. Flame* **2014**, *161*, 3201−3210.
(45) Minutolo, P.; Commodo, M.; Santamaria, A.; De Falco, G.; D'Anna, A. *Carbon* **2014**, *68*, 138−148.
(46) Ferrari, A. C.; Robertson, J. *Phys. Rev. B: Condens. Matter Mater. Phys.* **2000**, *61*, 14095−14107.
(47) Casiraghi, C.; Piazza, F.; Ferrari, A. C.; Grambole, D.; Robertson, J. *Diamond Relat. Mater.* **2005**, *14*, 1098−1102.
(48) McEnally, C. S.; Köylü, Ü. Ö.; Pfefferle, L. D.; Rosner, D. E. *Combust. Flame* **1997**, *109*, 701−720.

DOI: 10.1021/acs.energyfuels.7b01674
Energy Fuels 2017, 31, 10158−10164